



Oxygen vacancy induced defect dipoles in BiVO_4 for photoelectrocatalytic partial oxidation of methane

Received: 14 April 2024

Accepted: 11 October 2024

Published online: 23 October 2024



Xianlong Li^{1,6}, Zhiliang Wang^{1,6} , Alireza Sasani², Ardeshtir Baktash¹, Kai Wang¹, Haijiao Lu¹, Jiakang You¹, Peng Chen¹, Ping Chen¹, Yifan Bao¹, Shujun Zhang³, Gang Liu^{4,5} & Lianzhou Wang¹ 

A strong driving force for charge separation and transfer in semiconductors is essential for designing effective photoelectrodes for solar energy conversion. While defect engineering and polarization alignment can enhance this process, their potential interference within a photoelectrode remains unclear. Here we show that oxygen vacancies in bismuth vanadate (BiVO_4) can create defect dipoles due to a disruption of symmetry. The modified photoelectrodes exhibit a strong correlation between charge separation and transfer capability and external electrical poling, which is not seen in unmodified samples. Applying poling at -150 Volt boosts charge separation and transfer efficiency to over 90%. A photocurrent density of 6.3 mA cm^{-2} is achieved on the photoelectrode after loading with a nickel-iron oxide-based cocatalyst. Furthermore, using generated holes for methane partial oxidation can produce methanol with a Faradaic efficiency of approximately 6%. These findings provide valuable insights into the photoelectrocatalytic conversion of greenhouse gases into valuable chemical products.

Solar energy conversion via photoelectrocatalysis (PEC) plays a vital role in producing solar fuels toward carbon neutralization. Semiconductor materials such as Si, BiVO_4 and Fe_2O_3 as promising candidates have been investigated intensively, but low solar conversion efficiency is still the key challenge for the PEC process. To achieve high efficiency, effective charge separation and transfer (CST) of the photogenerated electron-hole pairs in the photoelectrodes is a prerequisite for subsequent surface reactions^{1,2}. Generally, the CST process occurs in the space charge layer due to the band bending at the interface of electrolyte and semiconductor based photoelectrodes³. However, the width of the space charge layer is smaller than the typical light penetration

depth in a semiconductor, leading to the recombination of a large proportion of the photogenerated electron-hole pairs, limiting the solar conversion efficiency^{1,4}. Building an internal electric field (IEF) is an effective way to provide additional driving force for the CST in a semiconductor^{5–7}. Semiconductors with well-aligned dipole moments, such as ferroelectric materials, normally show strong IEFs^{6,8}, however, their large bandgap and high resistance prevent the ferroelectric based photoelectrodes from obtaining good solar energy conversion efficiency⁹. While for commonly studied narrow bandgap semiconductor materials, such as BiVO_4 and Fe_2O_3 ^{10,11}, how to create an IEF in the materials remains challenging.

¹Nanomaterials Centre, School of Chemical Engineering, Australian Institute for Bioengineering and Nanotechnology, The University of Queensland, St Lucia, QLD 4072, Australia. ²CESAM QMAT Physique Théorique des Matériaux, Université de Liège, Liège, Belgium. ³Institute for Superconducting and Electronic Materials, Faculty of Engineering and Information Sciences, University of Wollongong, New South Wales 2500, Australia. ⁴Shenyang National Laboratory for Materials Science, Institute of Metal Research, Chinese Academy of Sciences, 72 Wenhua Road, Shenyang 110016, China. ⁵School of Materials Science and Engineering, University of Science and Technology of China, 72 Wenhua Road, Shenyang 110016, China. ⁶These authors contributed equally: Xianlong Li, Zhiliang Wang. ✉ e-mail: zhiliang.wang@uq.edu.au; l.wang@uq.edu.au

Since the IEF is produced from well-aligned dipole moments in bulk materials, it is critical to create dipole moment along a specific direction in a photoelectrode. Dipole moment is typically produced by the displacement of positive charge centers and negative charge centers¹². For many semiconductors, however, they have a high symmetry nature with inversion center (*i*-center), forbidding the generation of net dipole moments^{4,13}. In order to produce dipole moments, we need to locally break the inversion symmetry of lattice in a semiconductor^{14,15}. Creating defect structure is an efficient way to break the symmetry, wherein a defect dipole can be expected^{13–16}, as evidenced by the bulky dipole moment generated via Mg doping in the rutile TiO₂ lattice or Li-insertion in TiO₂ nanotube based photoelectrodes^{15,17}. In addition to foreign species doping, vacancies, such as oxygen- and metal- vacancies, are also important defects widely applied in modifying photoelectrodes^{8,16,18}. However, the question that how can the vacancy-induced defect dipoles be rationally tuned to facilitate the CST process in photoelectrodes remains unanswered.

In addition to the CST engineering in the PEC system, the optimization of surface reaction for utilizing the photogenerated charge carriers is equally important to achieve good PEC conversion efficiency. The reductive photogenerated electrons have found diverse applications including green hydrogen generation^{19,20}, carbon dioxide fixation^{21,22}, ammonium synthesis and others^{23,24}. However, the use of oxidative photogenerated holes for valuable chemical products

generation has received much less attention²⁵. Herein, we demonstrate that creating oxygen vacancies in metal oxide photoelectrodes can induce substantial amount of defect dipoles, which results in remarkable polarization behavior upon external poling, which are not achievable at the pristine photoelectrodes. By aligning the dipole moments with external poling treatment, exemplified using BiVO₄ photoelectrode, we are able to achieve a drastic improvement of CST photocurrent density (j_{CST}) by over 50%. The vacancies induced defect dipoles and unexpected polarization behavior are further verified to be a universal feature at different metal oxide based semiconductors. In addition, we demonstrate that the loading of NiFe-oxide cocatalyst on the polarized BiVO₄ photoelectrode can boost the photocurrent density to above 6 mA cm⁻² for partial oxidation of methane to methanol production, with a Faradic efficiency (FE) of *c.a.* 6%, highlighting the value-added utilization of the photogenerated holes.

Oxygen vacancy induced defect dipole

As a typical candidate in PEC research, pristine BiVO₄ is lack of dipole moment due to the presence of *i*-center in the structure (Fig. 1a)²⁶. Once oxygen vacancies (V_{O}) are introduced after an optimization of the V_{O} sites and structure reorganization, our simulation results indicate that the redistribution of electron cloud around metals and oxygen occurs, with a displacement between positive charges and negative charges, as illustrated in Fig. 1b. By comparing the distance of Bi-O and V-O pairs in the structure (Fig. 1c and Tables S1-2), it is evident

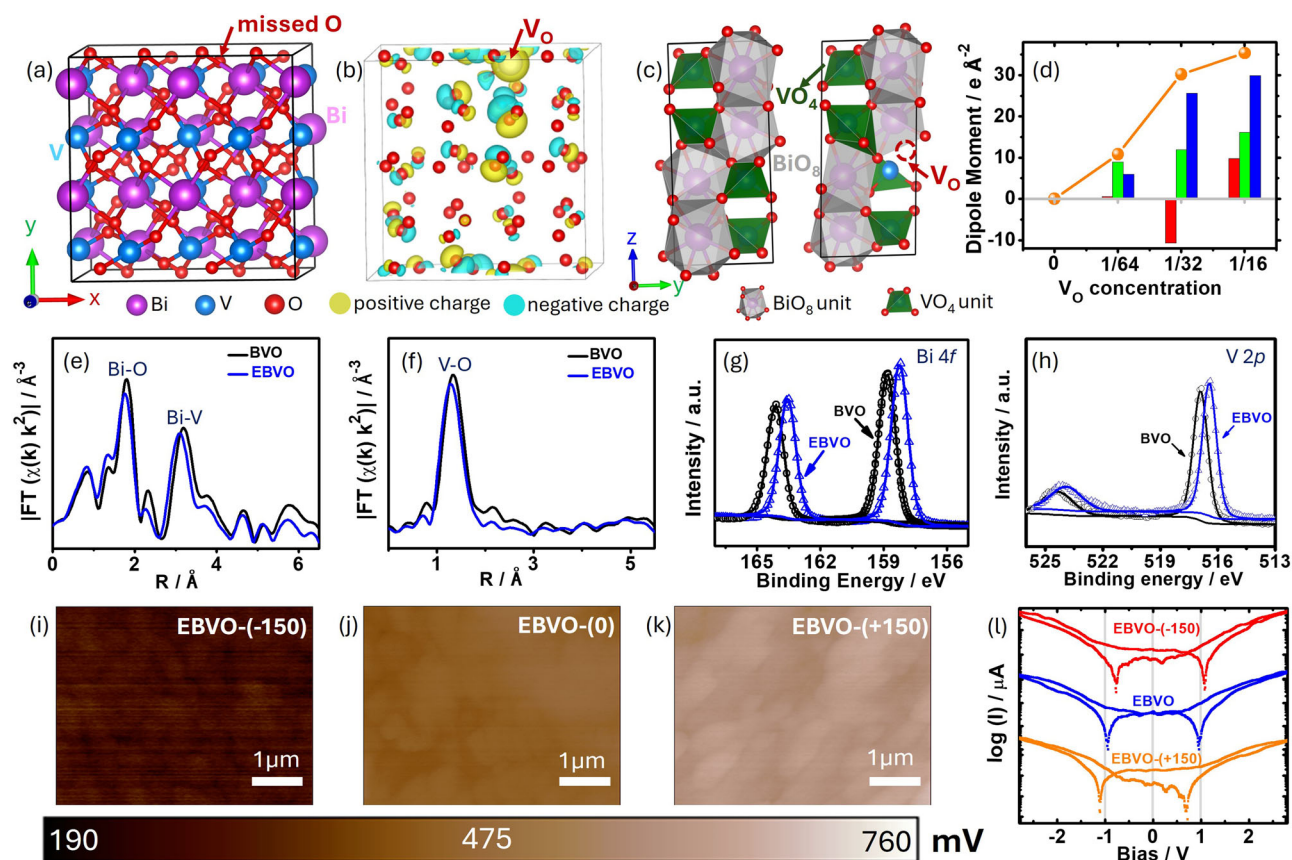


Fig. 1 | The formation of oxygen vacancies induced defect dipoles. **a** The structure of BiVO₄ crystal showing a missed O site for V_{O} . The Bi, V and O atoms are indicated as balls in purple, blue and red colors, respectively. **b** The charge density difference of BiVO₄ with V_{O} . The Bi and V atoms are hidden for clear visibility of the charge distribution in the BiVO₄, leaving O atoms (red balls) at their lattice sites. The V_{O} site is indicated with a gray ball. The yellow and cyan spheres indicate the positive and negative charges. **c** The BiVO₄ crystal with VO_4 (green) and BiO_8 (gray) units in pure and V_{O} modified structures. **d** The calculated dipole moment in BiVO₄

with different V_{O} concentrations. The dipole moment vectors of (*x*, *y*, *z*) are plotted in red, green and blue bars, and the vector modules are plotted in orange balls. **e**, **f** The k^2 -weighted EXAFS structure of Bi $L_{3\text{-edge}}$ and V K -edge with Fourier transforms for BVO (black) and EBVO (blue). **g**, **h** The fine structure of the XPS of Bi 4f and V 2p. **i–k** The surface potentials of EBVO film upon external poling at -150 V, 0 V and +150 V, respectively. The scale bar is 1 μm . **l** The I - V curves of EBVO under polarization at different voltages.

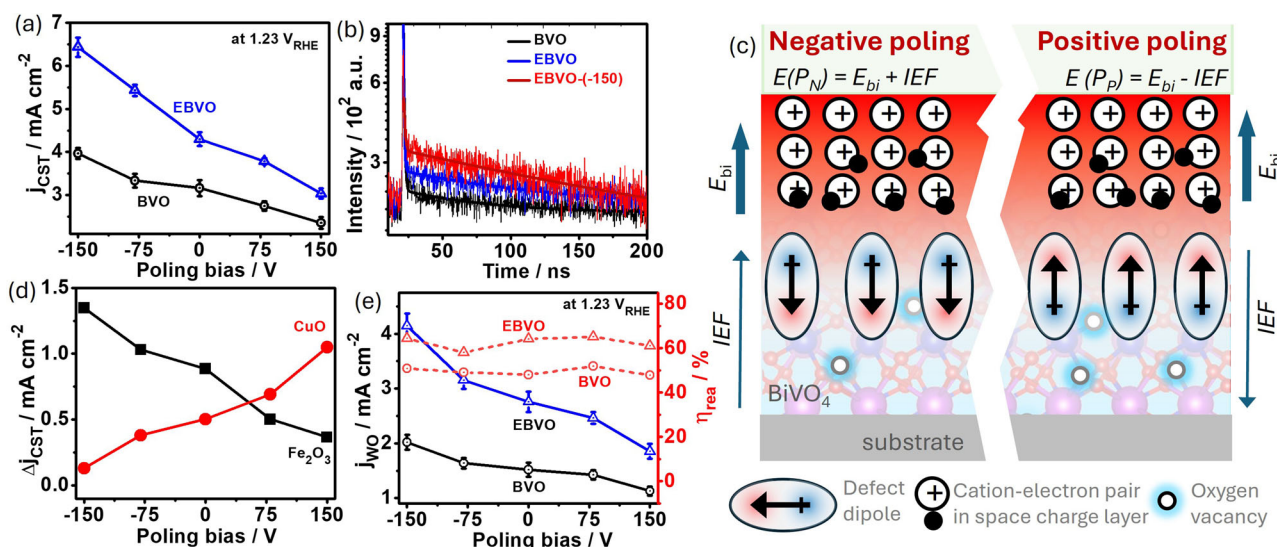


Fig. 2 | The defect dipoles tuned PEC performance. **a** The charge separation and transfer photocurrent density (j_{CST}) at 1.23 V_{RHE} for BVO and EBVO poled at different external bias. Error bars are presented for an average of three measurements for each data point. **b** The TRPL for BVO (black), EBVO (blue) and EBVO(-150) (red) samples. **c** The schematic illustration on how the IEF induced by external poling will modulate the total driving force (E_{total}) for CST process. The cation (+) and electron

(•) pairs are used to schematically show how the space charge layer is created with the E_{bi} . **d** The change of j_{CST} under different poling biases for Fe₂O₃ with V_O and CuO with V_{Cu}. **e** The water oxidation photocurrent density (j_{WO}) and the surface reaction efficiency (η_{rea}) of BVO and EBVO under different poling biases. Error bars are presented for an average of three measurements for each data point.

that the introduction of V_O breaks the symmetry in the VO₄ and BiO₈ polyhedrons. Additionally, by comparing the lattice parameters (a , b and c) of the unit cell in Fig. S1, it is clear there is a reduction in b and c , accompanied by an expansion in a . The structure asymmetry and electrons redistribution will establish dipoles. To quantify the impact of V_O on the formation of dipoles, we calculated the dipole moments of BiVO₄ with a V_O concentration of 0–6.25 at. % using the Berry phase approach^{27,28}. The results show that the pristine BiVO₄ exhibits no dipole moment, while increasing the V_O concentration leads to a gradual enhancement of the dipole moment (Fig. 1d and Table S3).

To validate the calculation prediction, pristine BiVO₄ photoelectrode is prepared via a calcination of BiOI and VOSO₄ precursors (sample noted as BVO)²⁹, followed by an electrochemical reduction to create V_O in the BiVO₄ (sample noted as EBVO)³⁰. Compared to the pristine BVO, the EBVO did not show obvious difference in terms of their appearance, micro-morphology and crystal phase as indicated in Figs. S2–4. But the microstructure and electronic status have some changes. From the extended X-ray absorption fine structure (EXAFS) of Bi L₃-edge (Fig. 1e) and V K-edge (Fig. 1f) analysis, similar Bi–O distance (1.81 Å for BVO *vs.* 1.79 Å for EBVO) and V–O distance (1.35 Å for BVO *vs.* 1.30 Å for EBVO) are observed in both samples. Interestingly, there is an obvious reduction of the Bi–V distance, from 3.19 Å for BVO to 3.09 Å for EBVO, which is in a good agreement with the predicted V_O induced structure shrinkage, as illustrated in Fig. 1c and Table S5. Due to the charge compensation during V_O formation, the V_O sites are positively charged (*i.e.*, less electrons) with the adjacent metal sites becoming negatively charged (*i.e.*, more electrons on Bi and V)³¹. The increased electron densities on Bi and V lead to the binding energy shifting toward low energy region, as shown in the corresponding X-ray photoelectron spectra in Fig. 1g, h and Fig. S5. The X-ray absorption spectra of Bi and V also indicate an edge shift toward increased electron density (Fig. S6). Based on the above characterizations and calculations in crystal structure and electronic structure, it is clear that V_O exists in the EBVO photoelectrodes, leading to the breaking of crystal symmetry and redistribution of electron cloud, which subsequently results in the formation of defect dipoles, as will be discussed below.

As a vector feature, the dipole orientation can be tuned along an external electric field^{7,12}. We further investigate the defect dipole

behavior by poling treatment of the EBVO photoelectrodes with an external bias (the samples are noted as EBVO-(x), here x represents the external bias between -150 V and +150 V) in Fig. 1i, k. From the surface potential image of the pristine EBVO (average 447.0 ± 42.7 mV, Fig. 1j), it is clear that negative poling, *i.e.*, EBVO(-150), reduces the surface potential to -289.3 ± 36.2 mV (Fig. 1i), while positive poling, EBVO(+150), increases it to 598.5 ± 79.6 mV (Fig. 1k). This result is similar to the behavior observed in typical ferroelectric BiFeO₃ photoelectrodes which possess intrinsic dipoles⁷. Of particular importance is that due to the relatively flexible feature of the defect dipoles induced by electron cloud displacement (Fig. 1b), the positive end of the dipole will stay at low potential position and negative end stays high when subjected to an external electric field. For the EBVO with defect dipoles, an electric field pointed from photoelectrode surface to the substrate will be built up at -150 V poling, wherein it will shift the defect dipoles with negative ends toward surface, therefore decrease the surface potential. Moreover, the well-aligned defect dipoles will generate a depolarized electric field across the whole film thickness (around 580 nm in Fig. S3), which is in an opposite direction of the external poling electric field^{7,9}. Once the external poling field is diminished, the depolarized electric field remains, resulting in a potential difference (ΔE , that is IEF) between the top surface and bottom of the EBVO film, as illustrated in Fig. S7. The hypothesis is confirmed by the microprobe testing results in Fig. 1l^{17,32}. According to the butterfly curves, the symmetric axis of the undershoots of the two wings signifies the ΔE across the film (Fig. S7). The pristine EBVO shows no discernible potential difference between the bottom and surface due to the negligible net dipole moment (Fig. 1l). While upon external poling, the randomly distributed dipole moments are effectively aligned, leading to the establishment of the IEF (*i.e.*, ΔE). Note that the external poling at negative bias results in a positive IEF directed from bottom to surface of the photoelectrode film, while opposite tendency is observed in the samples with positive poling (Fig. S7). These results clearly verify our hypothesis that IEF can be created in the vacancy containing EBVO photoelectrodes upon poling treatment.

To unveil the relationship between the IEF and CST property of the photoelectrodes, water oxidation performance is investigated, as illustrated in Fig. 2. For the pristine BVO and EBVO (*i.e.*, no external

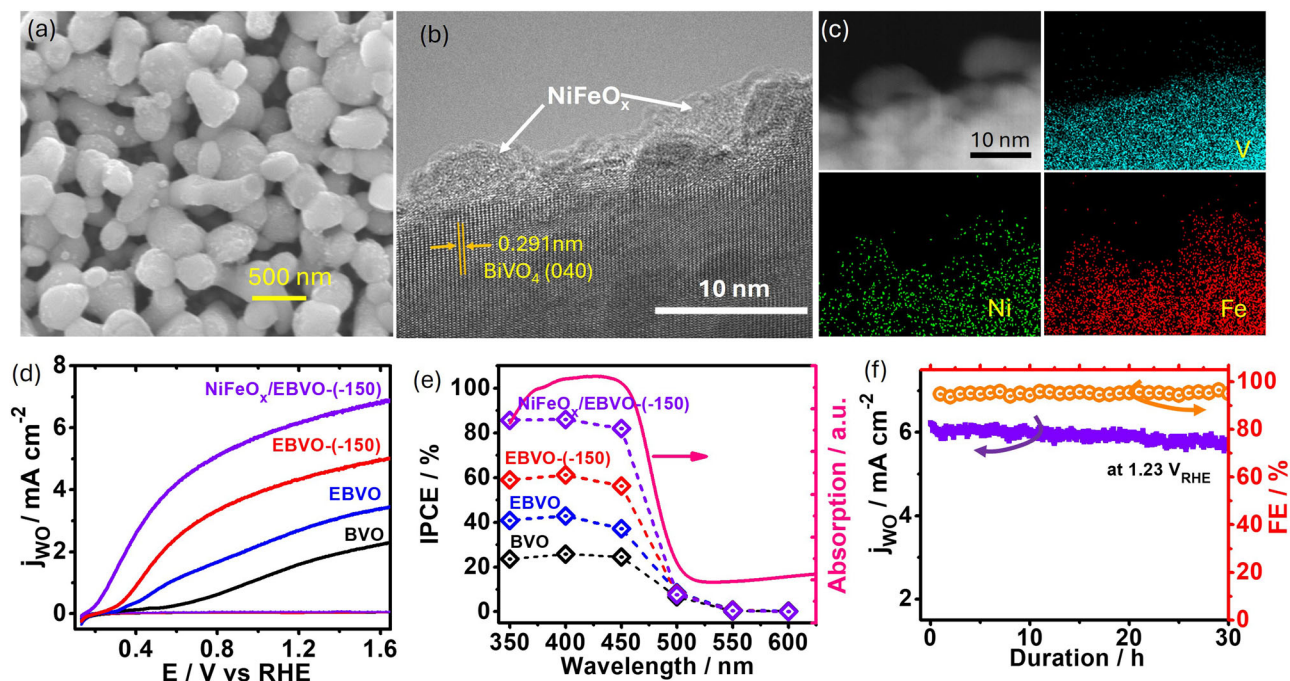


Fig. 3 | The water oxidation performance of NiFeO_x/EBVO photoelectrodes. **a** The morphology of NiFeO_x/EBVO(-150) photoelectrode. **b** The HRTEM of the NiFeO_x amorphous layer on EBVO(-150). **c** The elemental mapping of V, Ni and Fe in NiFeO_x/EBVO(-150). **d** and **e** The water oxidation photocurrent densities and the corresponding IPCEs at 1.23 V_{RHE} for BVO (black), EBVO (blue), EBVO(-150) (red),

and NiFeO_x/EBVO(-150) (purple) photoelectrodes. The light absorption of BiVO₄ (pink, indicated by arrow) is displayed for comparison in **e**. **f** The stability (purple) and the corresponding FE of oxygen (orange) on NiFeO_x/EBVO(-150) photoelectrodes tested at 1.23 V_{RHE}.

poling) in Fig. 2a, the introduction of V_O into BVO promotes the CST photocurrent density (j_{CST}) from 3.2 mA cm⁻² to 4.3 mA cm⁻² at 1.23 V vs Reversible Hydrogen Electrode (V_{RHE}), confirming the contribution of V_O in promoting the CST³⁰. Impressively, the j_{CST} can be further improved to 6.6 mA cm⁻² upon -150 V poling treatment, which is nearly double that of the BVO. On the other hand, when the EBVO is treated with a +150 V poling, its j_{CST} decreases to 3.0 mA cm⁻², fully eliminating the benefit of V_O . This result indicates that the PEC behavior of V_O containing photoelectrodes largely depends on the poling treatment history.

The photogenerated charge carrier dynamics is also investigated via the time-resolved photoluminescence (TRPL, Fig. 2b), where the decay curves are fitted by a bi-exponential function of time with all the fitted parameters summarized in Table S5. The fast decay component (τ_1) is associated with the surface recombination, while the slow decay (τ_2) can be assigned to the charge carrier recombination in the bulk BiVO₄ thin films³³. The fitted TRPL results indicates that the introduction of V_O prolongs the charge carrier lifetime in the bulk crystals with an almost doubled τ_2 , thereby yielding an increased average lifetime (τ_{avg}) of the photogenerated charge carriers from 50.83 ns to 107.81 ns (Table S5). By further applying a negative poling (P_N, i.e., polarization electric field points from surface of BiVO₄ film to substrate) of -150 V to the EBVO, the τ_{avg} can be significantly improved to 243.72 ns (Table S5). However, when positively poled (P_P, i.e., polarization electric field points from substrate to surface of BiVO₄ film) at +150 V, the charge carrier's lifetime of the EBVO(+150) decreases to 77.49 ns as indicated in Table S5 and Fig. S8. These results further indicate that P_N treatment extends the photogenerated charge carrier's lifetime for the improved CST process, well aligning with the observed results in the CST measurement (Fig. 2a).

In the BiVO₄ photoelectrodes, the CST process is driven by the electric field established at the BiVO₄/electrolyte interface and within the films. As shown in Fig. 2c, a built-in electric field (E_{bi}) is established at space charge layer of the interface, with its direction toward the

surface due to the band bending³⁴. But inside the bulk, the orientation of IEF induced by defect dipoles can be tuned under external poling. Therefore, the CST driving force (E_{total}) is dominated by the sum of E_{bi} and IEF, wherein IEF is modulated with the poling treatment as shown in Fig. 2c. According to our previous research on ferroelectric photoelectrode⁷, the IEF is aligned with the E_{bi} at a P_N case, therefore the E_{total} for the CST process is an add-up of E_{bi} and IEF (Fig. 2c). However, under P_P, the IEF will be directed against E_{bi} , so E_{total} for the CST process is a deduction of E_{bi} by the IEF, leading to a weakened CST process^{7,35}. The modulated CST process by external poling is further confirmed by the charge transfer resistance and open circuit potential tests in Fig. S9.

Considering the negligible dipole moment predicted in pristine BVO (Fig. 1d), it is interesting to find that the j_{CST} of BVO also shows a response to external poling, as illustrated in Fig. 2a. However, compared to EBVO, the BVO presents a much smaller slope of j_{CST} -poling bias curves. The relatively sluggish j_{CST} change upon external poling is possibly due to the much less V_O concentration in pristine BVO. From the Mott-Schottky (M-S) curves in Fig. S10, BVO shows a typical n-type semiconductor with a positive slope of M-S curves. It is generally recognized that the n-type conductivity of metal oxide is originated from its unavoidable V_O during material synthesis³¹. The presence of V_O in BVO also produces defect dipoles and responds to external poling treatment as shown in Fig. 2a. By increasing the concentration of V_O , a reduced slope of M-S curve is observed, suggesting a higher V_O concentration in EBVO (Fig. S10). The high V_O concentration leads to increased defect dipole moments, therefore exhibiting a more pronounced response to external poling, as observed in Fig. 2a.

In fact, oxygen vacancies are common in many metal oxides and can be induced in different methods, therefore we expect that similar behaviors should be observed in different types of oxide based photoelectrodes. For the BiVO₄ used here, when V_O is created via a heat treatment, we can also observe nearly the same response of j_{CST} to external poling treatment as shown in Fig. S11. This result further

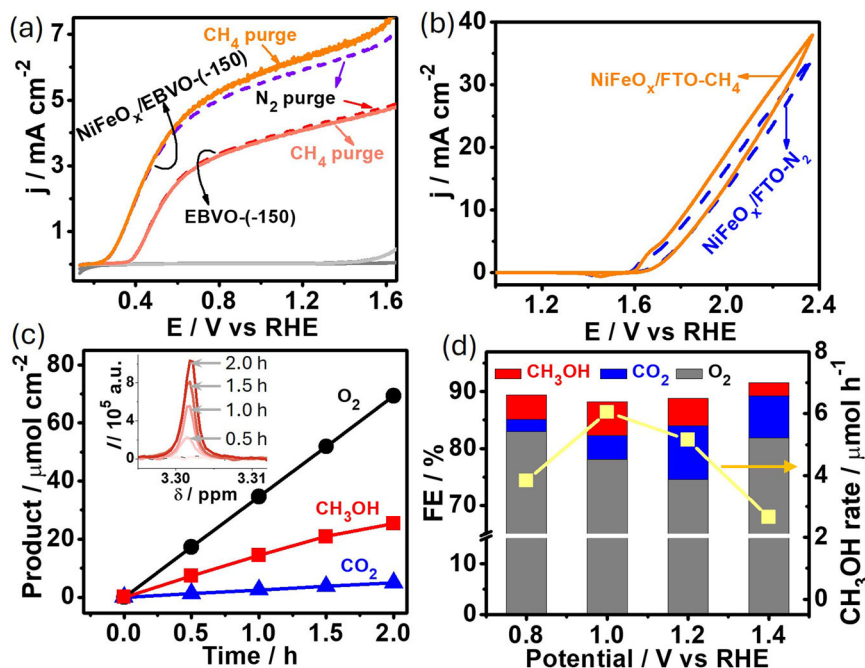


Fig. 4 | The methane partial oxidation on NiFeO_x/EBVO(-150) photoelectrodes. **a** The comparison of photocurrent density of NiFeO_x/EBVO(-150) and EBVO(-150) photoelectrodes under CH₄ flow (solid line) and N₂ flow (dash line). **b** The electrocatalytic performance of CH₄ oxidation on NiFeO_x/FTO electrode. **c** The products of O₂, CH₃OH and CO₂ during PEC test of NiFeO_x/EBVO(-150) photoelectrode

at 1.2 V_{RHE} under CH₄ flow. The inset shows hydrogen nuclear magnetic resonance (H-NMR) signal of CH₃OH (δ = 3.30 ppm) intensity (I) change with the reaction time. **d** The FE of produced O₂ (gray) CH₃OH (red) and CO₂ (blue) at different PEC testing potentials on NiFeO_x/EBVO(-150) photoelectrode. The CH₃OH production rates at different potentials are indicated by yellow data points.

confirms that it is the V_O , not the treatment method, that leads to the poling response of a photoelectrode. With this knowledge, we further explore the vacancies' influence to other photoelectrodes. Taking the hematite (*i.e.* Fe₂O₃) as an example, the V_O tuning has been reported in modifying n-type Fe₂O₃ photoelectrodes (Fig. S12a)³¹. We found that both the pristine and V_O -Fe₂O₃ photoelectrodes exhibit a tunable photocurrent density upon external poling treatment (Fig. S13a). When comparing the photocurrent change (Δj_{CST}) of Fe₂O₃ upon poling, a reduced Δj_{CST} along with the increased poling bias is observed (Fig. 2d), similar to the tendency observed in BiVO₄ (Fig. S14). In addition to oxygen vacancies, previous studies have also confirmed that metal vacancies, such as Cu vacancies (V_{Cu}), can be produced in p-type CuO photoelectrodes³⁶. With the creation of additional V_{Cu} in CuO photoelectrode (Fig. S12b), the j_{CST} and corresponding Δj_{CST} exhibit a gradual increase with the external poling, as revealed in Fig. 2d and Fig. S12b. These results indicate that an opposite polarization behavior (j_{CST} -poling bias curves) between Fe₂O₃ and CuO has been observed. That may originate from the intrinsic difference in defect dipoles as the charging states of V_O in Fe₂O₃ and V_{Cu} in CuO are different. Specifically, V_O carries a positive charge (Fig. S13c, fewer electrons), whereas V_{Cu} bears a negative charge (Fig. S13d, more electrons)^{31,36,37}. As a result, the defect dipole vectors in Fe₂O₃ and CuO exhibit distinct orientations, as depicted in Fig. S13. This disparity results in opposite reactions to external poling in Fig. 2d. Above all, the tunable photocurrent response to external poling in different photoelectrodes confirms that the defect dipole alignment can be a generic feature in metal oxide semiconductors.

Defect dipoles promoted photoelectrocatalysis

The tuned j_{CST} shows a straightforward influence on its water oxidation performance as shown in Fig. 2e. The pristine BVO has a water oxidation photocurrent density (j_{WO}) of 1.5 mA cm⁻² at 1.23 V_{RHE}. By introducing the V_O , the EBVO photoelectrode achieves a j_{WO} of 2.7 mA cm⁻². Poling the EBVO at -150 V further boosts the j_{WO} to above 4.0 mA cm⁻². Taking the j_{CST} into consideration, we can calculate the surface

reaction efficiency ($\eta_{rea} = j_{WO}/j_{CST}$) change with the external poling bias³⁸. As illustrated in Fig. 2e, the η_{rea} does not show significant change upon poling. This finding suggests that poling treatment majorly affects the bulky CST, while has limited influence on the surface reaction. Comparing to the nearly 90% CST efficiency (η_{CST} , Fig. S15), the <50% η_{rea} indicates there is a significant recombination of photo-generated charges at the surface due to the slow reaction kinetics of the four-charge involved water oxidation.

To address this challenge, we further deposit low-cost nickel-iron oxide based surface cocatalyst (noted as NiFeO_x) on the BiVO₄ photoelectrodes. Despite the absence of NiFeO_x signal in XRD patterns (Fig. S16), the presence of NiFeO_x species is confirmed by X-ray photoelectron spectroscopies (Fig. S17). Due to the thin nature of the NiFeO_x layer, the surface structure of the original BiVO₄ photoelectrode is not significantly altered, as shown in the SEM images (Fig. 3a, Fig. S3). From the high-resolution transmission electron microscope (HRTEM) and the corresponding elemental mapping of Ni and Fe, an amorphous NiFeO_x coating layer is visualized on the surface of BiVO₄ photoelectrodes (Fig. 3b, c). The introduction of NiFeO_x considerably improves the surface reaction efficiency to nearly 90% (Fig. S15). Due to the synergistic contributions from the defect dipole and cocatalyst NiFeO_x, the optimized NiFeO_x/EBVO(-150) achieves a j_{WO} of 6.3 mA cm⁻² at 1.23 V_{RHE} with a small onset potential of around 0.2 V_{RHE} (Fig. 3d and Figs. S8), which is comparable to the champion BiVO₄ photoelectrodes for water oxidation as tabulated in Table S6. The corresponding incident photon-to-current efficiency (IPCE) exceeding 80% is achieved, with the IPCE-wavelength action curve closely aligning with the absorption curve of BiVO₄ (Fig. 3e). Encouragingly, the NiFeO_x/EBVO(-150) photoelectrode demonstrates a good stability of over 30 h, coupled with an excellent O₂-Faradaic efficiency (FE) of over 95% (Fig. 3f) and minor surface changes (Fig. S3). The electrochemical testing about the NiFeO_x on various BiVO₄ photoelectrodes have shown the advantage of NiFeO_x in promoting water oxidation (Figs. S19, 20) and preventing BiVO₄ from corrosion or structure corruption (Figs. S20–23). These results indicate that NiFeO_x layer can

effectively utilize photogenerated holes for water oxidation while shielding the BiVO₄ photoelectrode from holes induced photocorrosion. But due to the metastable intrinsic feature of the aligned dipoles, they will relax during storage, leading to decay of photocurrent improvement as shown in Fig. S26. This process can be recovered and well matches our recent finding in the ferroelectric BiFeO₃ system³⁸.

To make good use of the photogenerated holes on the photoelectrodes, we further consider to extend the water oxidation ($4\text{OH}^- + 4\text{h}^+ \rightarrow \text{O}_2 + 2\text{H}_2\text{O}$) to value-added reactions, such as methane conversion to valuable products (e.g., methanol via $\text{CH}_4 + 2\text{h}^+ + 2\text{OH}^- \rightarrow \text{CH}_3\text{OH} + \text{H}_2\text{O}$)^{39–41}. To investigate the feasibility of methane partial oxidation on the developed photoelectrodes, methane gas was purged into the PEC cell. It shows that the photocurrent density of NiFeO_x/EBVO(-150) photoelectrode has obviously increase with CH₄ purge compared to the N₂ purge (Fig. 4a). It is interesting that there is no obvious difference on EBVO(-150) with the absence of co-catalyst (Fig. 4a), further underlining the significance of NiFeO_x in methane activation. A similar CH₄ induced photocurrent increase is observed in NiFeO_x/BVO photoelectrode (Fig. S27), further confirm that CH₄ conversion is motivated by NiFeO_x other than the poling treatment. Subsequent electrocatalytic test of NiFeO_x deposited on the substrate of fluorene doped tin oxide (FTO) in a CH₄ flow indicates a significantly higher oxidative current in the presence of CH₄ flow (Fig. 4b). We then further study the methane oxidation products in both gas and liquid phases. At a testing potential of 1.2 V_{RHE}, the generation of oxygen, methanol and carbon dioxide with a gradual accumulation of the products is observed, as shown in Fig. 4c and Figs. S27, 28. Interestingly, only methanol as a liquid phase product is observed in the cell, evidenced by its typical chemical shift (δ) of 3.30 ppm (inset in Fig. 4c and Fig. S29)⁴². According to the photocurrent density (Fig. S30), we calculate the FE of methanol (FE(CH₃OH)) to be around 4.8%. We then further investigate the influence of applied potential on methanol production. As shown in Fig. 4d, the presence of methane can reduce the FE(O₂) to below 83% due to the presence of methane oxidation. The peak methanol production rate (6.04 $\mu\text{mol h}^{-1}$ with an area of 0.36 cm²) is achieved under a potential of 1.0 V_{RHE} with a c.a. 6% FE(CH₃OH), which represents as one of the most effective processes as shown in Table S7^{43,44}. The above results verify a value-added process for making better utilization of the photogenerated holes along with green hydrogen production. We can apply the defect dipoles to accelerate the bulky CST and use the surface cocatalyst to steer the surface reaction pathway, paving a way to the utilization of the photogenerated holes for CH₃OH production and electrons for hydrogen production.

In summary, we demonstrated that vacancies can induce defect dipoles in metal oxide semiconductors, and efficiently tune the charge separation and transfer process at the metal oxide semiconductor photoelectrodes. Using the BiVO₄ as an example, the defect dipoles drastically boost the charge separation and transfer efficiency under -150 V poling. By further introducing a surface cocatalyst of NiFeO_x, a water oxidation photocurrent density of 6.3 mA cm⁻² with a stability over 30 h is achieved. Moreover, the NiFeO_x/EBVO(-150) photoelectrode shows effective methane partial oxidation capability with a high methanol production. The findings provide a direction for rational design of photoelectrocatalytic reactions toward efficient solar driven greenhouse gas mitigation and valuable chemical production.

Methods

Materials

The following chemicals are used in the experiment, including Potassium iodide (KI, Sigma-Aldrich, ≥95%), Nitric acid (HNO₃, Merck, 69%), Bismuth nitrate pentahydrate (Bi(NO₃)₃·5H₂O, Sigma Aldrich, >98%), P-benzoquinone (Sigma-Aldrich, ≥98.0%), vanadyl (V) acetylacetonate (VO(acac)₂, Sigma-Aldrich, 99%), Dimethyl sulfoxide (DMSO, Sigma-

Aldrich, 99.9%), Boric acid (H₃BO₃, Sigma-Aldrich, 99.5%), Potassium hydroxide (KOH, Sigma-Aldrich 86%), Iron(II) sulfate heptahydrate (FeSO₄·7H₂O, Sigma-Aldrich, ≥99%), Nickel(II) sulfate hexahydrate (NiSO₄·6H₂O, Sigma-Aldrich, ≥98%) Iron(III) nitrate nonahydrate (Fe(NO₃)₃·9H₂O, Sigma-Aldrich, ≥98%) Absolute ethanol (CH₃OH, Merk, 99.9%), Copper(II) acetate monohydrate (Cu(CO₂CH₃)₂·H₂O, Chem-supply, ≥98%), Sodium sulfite (Na₂SO₃, Sigma-Aldrich, ≥98%), sodium hydroxide (NaOH, Sigma-Aldrich, ≥98%), Hydrogen peroxide (H₂O₂, Supelco, 30%), Sodium sulfate (Na₂SO₄, Sigma-Aldrich, ≥99%), Potassium persulfate (K₂S₂O₈, Sigma-Aldrich, ≥99%) and Deuterium oxide (D₂O, Sigma-Aldrich, 99.9%). All the chemicals are used as received without further purification.

BiVO₄ synthesis and electrochemical reduction treatment

The synthesis of BiVO₄ (BVO) photoelectrode was based on the reported work. 50 mL 0.4 M KI (pH 1.7) and 0.04 M Bi(NO₃)₃·5H₂O was mixed with 20 mL 0.23 M p-benzoquinone ethanol solution for BiOI electrodeposition on the Fluorine-doped tin oxide substrates (FTO) in a typical three-electrode system. The deposition was set at -0.15 V vs. Ag/AgCl for 240 s. Then, the V source of vanadyl acetylacetonate (VO(acac)₂) was loaded on BiOI films and calcinated in the muffle furnace at 450 °C for 2 h. The excess V₂O₅ on the BiVO₄ film was removed in 1 M NaOH solution.

Electrochemical reduction treatment for BVO photoelectrode was conducted in a three-electrode electrochemical cell where BVO film, saturated calomel electrode (SCE) and Pt electrode acted as the working, counter and reference electrode, respectively. A reduction treatment was applied to the BVO photoelectrode at -0.15 V_{RHE} for 120 s in 1 M borate buffer electrolyte (pH 9.5) (Fig. S33). Alternatively, the V_O was created by heating the as-prepared BiVO₄ photoelectrode in a pure nitrogen flow at 450 °C for 2 h in a tube furnace, noted as H-BVO.

The NiFeO_x electrocatalyst was loaded via a sequentially photo-assisted electrodeposition of FeO_x and NiO_x in a 0.1 M FeSO₄ solution at 0.25 V vs. Ag/AgCl for 20 min and in a 0.1 M NiSO₄ solution at 0.11 V vs. Ag/AgCl for 20 min. The NiFeO_x/FTO electrode was fabricated by electrodeposition at 1.2 V vs. Ag/AgCl (4 M KCl) for 30 min in a 0.1 M FeSO₄ solution and a 0.1 M NiSO₄ solution at 70 °C.

The Fe₂O₃ photoelectrode was fabricated through the spin coating method. Typically, 2 M Fe(NO₃)₃·9H₂O ethanol solution was spread on a FTO substrate spined at 2500 rpm for the 30 s. The spin-coating process was repeated 2 times and pre-annealed on a hotplate at 120 °C for 5 min, followed by further thermal treatment in a muffle furnace at 800 °C for 20 min. The V_O was created by calcinating the as-prepared Fe₂O₃ photoelectrode in a pure nitrogen flow at 600 °C for 4.0 h in a tube furnace.

The CuO photoelectrode was achieved from the oxidization of the Cu₂O electrode. The Cu₂O was deposited at -0.4 V vs SCE in 0.2 M copper acetate solution with a 3-electrode system for 15 min. Then, the Cu₂O film was converted into CuO film through an annealing at 450 °C for 2 h in air. The V_{Cu} on CuO photoelectrode was produced by heating the as-prepared Cu₂O photoelectrode in a pure oxygen flow at 450 °C for 2 h in a tube furnace.

Poling process

Poling treatment was carried out on a DC power source (ITECH DC POWER SUPPLY, IT6834) as shown in Fig. S31. A device composed of a Ti plate electrode and a bismuth vanadate photoelectrode was fabricated with the insulation from Kapton tape. Then poling bias of 0–150 V is loaded on the device for 30 min with the same polarity as previous work⁷. That is, when the photoelectrode is connected to the positive pole and Ti to the negative pole of the DC power source, the photoelectrode poling voltage is noted as positive. Otherwise, it is noted as negative.

Computational details

The polarization of BVO is calculated using the Vienna Ab Initio Package (VASP)^{45,46} and its projected augmented wave implementation of DFT²⁷. The PBEsol-GGA functional is selected for the exchange correlation functional²⁸. To sample the reciprocal lattice for both the primitive cell and the applied supercell, k-points of $6 \times 6 \times 4$ and $3 \times 3 \times 4$ are considered, respectively. The supercell is made of $2 \times 2 \times 1$ primitive cell. A cut-off energy on the plane-wave expansion of 600 eV was enough to converge our structures to $<10^{-3}$ Å in lattice parameters. The tolerance on force for relaxing the structure was set to 10^{-3} eV/Å. The calculation of the polarization is done using Berry phase^{47,48} as implemented in VASP. To visualize the structures, the VESTA software is employed in this article⁴⁹.

Materials characterizations

The morphology and crystal lattice of film photoelectrode were imaged with scanning electron microscope (SEM, JEOL JSM 7001F) and high-resolution transmission electron microscopy (HR-TEM, Hitachi HF5000). The crystal phase structure was characterized by X-ray diffraction (XRD) spectroscopy (Bruker D8 Advanced diffractometer) with Cu K α ($\lambda = 1.5418$ Å) radiation. The light absorbance spectrum was obtained by the ultraviolet–visible (UV–Vis) absorption spectra (JASCOV-650 spectrophotometer). The element chemical state was analyzed with X-ray photoelectron spectroscopy (XPS, Kratos Ultra) with a mono Al X-ray source. The X-ray absorption spectroscopy over the Bi L-edge and V K-edge was collected at the Australian Synchrotron. A commercial atomic force microscope (AFM, Cypher, Asylum Research) was used for surface potential measurement via Kelvin probe force microscopy (KPFM) and I–V curve via conductive AFM (C-AFM). The surface potential of the photoelectrode was acquired by KPFM with Pt-coated Si conductive probes (Olympus ASYELEC.01-R2, spring constant ~ 2.8 N m $^{-1}$ and tip radius ~ 28 nm) on under ambient conditions. During I–V curve measurement via C-AFM, bias was loaded via the Pt-coated Si conductive probe as shown in Fig. S7. The time-resolved PL decays were measured upon a 375 nm pulsed diode laser excitation (FLSP-900, Edinburgh Instruments).

Photoelectrochemical and electrochemical measurement for water splitting

Photoelectrochemical water splitting performance and Mott–Schottky (M–S) measurement were conducted on a CHI660E potentiostat. The charge separation and transfer (CST) efficiency of BiVO $_4$ -based photoelectrodes were evaluated in 1 M borate buffer electrolyte (pH 9.5) with 0.2 M Na $_2$ SO $_3$ as the hole scavenger. Their water-oxidation performance was measured in 1 M borate buffer electrolyte (pH 9.5). The M–S curves were measured at 1 kHz frequency in the 1 M borate buffer electrolyte (pH 9.5). For Fe $_2$ O $_3$ -based photoelectrodes, the CST capability and water-oxidation performance were investigated in 1.0 M NaOH solution with/without 0.1 M H $_2$ O $_2$ (pH 13.6) respectively. For CuO-based photocathodes, the CST ability was investigated in 0.5 M Na $_2$ SO $_4$ solution (pH 6.5) with 0.2 M K $_2$ S $_2$ O $_8$ as an electron scavenger. The open circuit potential (OCP) was conducted in 1 M borate buffer solution under dark and continuous illumination. The photoelectrochemical impedance spectrum (PEIS) was conducted at 0.4 vs SCE in 1 M borate buffer solution under continuous illumination within a frequency range of 10^{-2} – 10^6 Hz. For the PEC test, all the photoelectrodes are scanned in dark until it achieves stable photocurrent.

The potential versus SCE was scaled to RHE using the Nernst Eq. (1)^{50,51}:

$$E_{\text{RHE}} = E_{\text{SCE}} + 0.059 \times \text{pH} + 0.2411 \quad (1)$$

The incident-photon-to-current conversion efficiency (IPCE) for BiVO $_4$ -based photoelectrode was determined via an Oriel Cornerstone

260 1/4 m monochromator coupled with a 300 W Oriel Xe lamp as the simulated light source. IPCE was measured at 1.23 V $_{\text{RHE}}$ in 1 M borate buffer (pH 9.5) using the same electrochemical cell described above for photoresponse. The power density at a specific wavelength was calculated from the IPCE value of standard Si diode. IPCE values were calculated using the following Eq. (2)

$$\text{IPCE} = j \times 1240 / (\lambda \times P_{\text{light}}) \quad (2)$$

where j (mA cm $^{-2}$) presents the photoresponse for BiVO $_4$ photoelectrode under the light with a wavelength of λ at an intensity of P_{light} (mWcm $^{-2}$) at 1.23 V $_{\text{RHE}}$

Photoelectrochemical CH $_4$ oxidation measurement

The photoelectrochemical methane conversion process was conducted in the same reactor as the PEC water splitting. Methane conversion was performed in an H-type cell after purging CH $_4$ (10 mL min $^{-1}$) for 30 min in 1 M borate buffer solution (pH = 9.5). Subsequently, the photoelectrochemical methane oxidation was conducted at 0.8, 1.0, 1.2, 1.4 V $_{\text{RHE}}$ to analyze the products of CH $_4$ conversion and their corresponding Faradaic efficiencies (FEs). The liquid product (CH $_3$ OH) was analyzed through ^1H -NMR spectroscopy (Bruker Avance III HD 500 MHz spectrometer) with dimethyl sulfoxide as the internal standard in 10 % D $_2$ O using the water suppression mode. The gas products (O $_2$ and trace CO $_2$) from PEC CH $_4$ oxidation were detected via a gas chromatograph (GC, Shimadzu GC-2014C) equipped with a thermal conductivity detector (TCD) and a flame ionization detector (FID).

The Faradaic efficiency (FE) was calculated using following Eq. (3):

$$\text{FE} = \frac{Q_{\text{product}}}{Q_{\text{total}}} \times 100\% = \frac{n_{\text{product}} \times Z \times F}{j \times t} \times 100\% \quad (3)$$

where j is photocurrent density, t is reaction time, n_{product} is the molar amount of the corresponded product, Z is the charge transfer number ($Z = 4$ for H $_2$ O–O $_2$, $Z = 2$ for CH $_4$ –CH $_3$ OH, $Z = 8$ for CH $_4$ –CO $_2$) and F is the Faradaic constant (96,485 C mol $^{-1}$).

For the methanol produced in the electrolyte, its concentration (C_{MeOH}) is calculated from the relative peak area (A) in the ^1H -NMR compared to the DMSO according to Eq. (4):

$$C_{\text{MeOH}} = \frac{A_{\text{MeOH}}/3}{A_{\text{DMSO}}/6} \times C_{\text{DMSO}} \times 22.8 \quad (4)$$

The C_{DMSO} is 49.5 $\mu\text{mol L}^{-1}$, the methanol in the electrolyte has been diluted by 22.8 times in the NMR tube.

For the above electrocatalytic/photoelectrocatalytic measurements and electrodepositions, all the electrolytes were freshly prepared before use. No resistance (iR) correction was applied to the applied potential.

Data availability

All data generated or analysed during this study are included in the published article and its Supplementary Information and Source Data files. Source data are provided with this paper. Source Data file has been deposited in the Materials Cloud Archive under accession code DOI link of <https://archive.materialscloud.org/record/2024.145>.

References

- Cowan, A. J. & Durrant, J. R. Long-lived charge separated states in nanostructured semiconductor photoelectrodes for the production of solar fuels. *Chem. Soc. Rev.* **42**, 2281–2293 (2013).
- Zhang, P., Wang, T., Chang, X. & Gong, J. Effective charge carrier utilization in photocatalytic conversions. *Acc. Chem. Res.* **49**, 911–921 (2016).

3. Chen, R., Fan, F., Dittrich, T. & Li, C. Imaging photogenerated charge carriers on surfaces and interfaces of photocatalysts with surface photovoltage microscopy. *Chem. Soc. Rev.* **47**, 8238–8262 (2018).
4. Li, J. & Wu, N. Semiconductor-based photocatalysts and photoelectrochemical cells for solar fuel generation: a review. *Catal. Sci. Tech.* **5**, 1360–1384 (2015).
5. Liu, Y. et al. Internal-field-enhanced charge separation in a single-domain ferroelectric PbTiO_3 photocatalyst. *Adv. Mater.* **32**, 1906513 (2020).
6. Wan, G. et al. Photocatalytic overall water splitting over PbTiO_3 modulated by oxygen vacancy and ferroelectric polarization. *J. Am. Chem. Soc.* **144**, 20342–20350 (2022).
7. Li, X. et al. Polarization alignment in polycrystalline BiFeO_3 photoelectrodes for tunable band bending. *ACS Nano* **17**, 22944–22951 (2023).
8. Cockayne, E. & Burton, B. P. Dipole moment of a Pb–O vacancy pair in PbTiO_3 . *Phys. Rev. B* **69**, 144116 (2004).
9. Li, Y., Li, J., Yang, W. & Wang, X. Implementation of ferroelectric materials in photocatalytic and photoelectrochemical water splitting. *Nanoscale Horizons* **5**, 1174–1187 (2020).
10. Kim, J. H. & Lee, J. S. Elaborately modified BiVO_4 photoanodes for solar water splitting. *Adv. Mater.* **31**, 1806938 (2019).
11. Sivula, K., Le Formal, F. & Grätzel, M. Solar water splitting: progress using hematite ($\alpha\text{-Fe}_2\text{O}_3$) photoelectrodes. *ChemSusChem* **4**, 432–449 (2011).
12. Chen, F., Huang, H., Guo, L., Zhang, Y. & Ma, T. The role of polarization in photocatalysis. *Angew. Chem. Int. Ed.* **58**, 10061–10073 (2019).
13. Park, D.-S. et al. Induced giant piezoelectricity in centrosymmetric oxides. *Science* **375**, 653–657 (2022).
14. Huangfu, G. et al. Giant electric field-induced strain in lead-free piezoceramics. *Science* **378**, 1125–1130 (2022).
15. Dong, W. et al. Collective nonlinear electric polarization via defect-driven local symmetry breaking. *Mater. Horizons* **6**, 1717–1725 (2019).
16. Wang, Z., Xiao, M., You, J., Liu, G. & Wang, L. Defect engineering in photocatalysts and photoelectrodes: from small to big. *Acc. Mater. Res.* **3**, 1127–1136 (2022).
17. Hu, Y. et al. Lattice distortion induced internal electric field in TiO_2 photoelectrode for efficient charge separation and transfer. *Nat. Commun.* **11**, 1–10 (2020).
18. Cezar, A. B., Graff, I. L., Varalda, J., Schreiner, W. H. & Mosca, D. H. Oxygen-vacancy-induced room-temperature magnetization in lamellar V_2O_5 thin films. *J. Appl. Phys.* **116**, 163904 (2014).
19. Wang, Q. & Domen, K. Particulate photocatalysts for light-driven water splitting: mechanisms, challenges, and design strategies. *Chem. Rev.* **120**, 919–985 (2019).
20. Wang, Q. et al. Scalable water splitting on particulate photocatalyst sheets with a solar-to-hydrogen energy conversion efficiency exceeding 1%. *Nat. Mater.* **15**, 611–615 (2016).
21. Fang, S. et al. Photocatalytic CO_2 reduction. *Nat. Rev. Methods Primers* **3**, 61 (2023).
22. White, J. L. et al. Light-driven heterogeneous reduction of carbon dioxide: photocatalysts and photoelectrodes. *Chem. Rev.* **115**, 12888–12935 (2015).
23. Kim, S., Park, Y., Kim, J., Pabst, T. P. & Chirik, P. J. Ammonia synthesis by photocatalytic hydrogenation of a N_2 -derived molybdenum nitride. *Nat. Synth.* **1**, 297–303 (2022).
24. Guan, Y. et al. Light-driven ammonia synthesis under mild conditions using lithium hydride. *Nat. Chem.* **16**, 1–7 (2024).
25. Wang, S., Liu, G. & Wang, L. Crystal facet engineering of photoelectrodes for photoelectrochemical water splitting. *Chem. Rev.* **119**, 5192–5247 (2019).
26. Tokunaga, S., Kato, H. & Kudo, A. Selective preparation of monoclinic and tetragonal BiVO_4 with scheelite structure and their photocatalytic properties. *Chem. Mater.* **13**, 4624–4628 (2001).
27. Blöchl, P. E. Projector augmented-wave method. *Phys. Rev. B* **50**, 17953 (1994).
28. Perdew, J. P. et al. Restoring the density-gradient expansion for exchange in solids and surfaces. *Phys. Rev. Lett.* **100**, 136406 (2008).
29. Kim, T. W. & Choi, K.-S. Nanoporous BiVO_4 photoanodes with dual-layer oxygen evolution catalysts for solar water splitting. *Science* **343**, 990–994 (2014).
30. Wang, S., Chen, P., Yun, J. H., Hu, Y. & Wang, L. An electrochemically treated BiVO_4 photoanode for efficient photoelectrochemical water splitting. *Angew. Chem.* **129**, 8620–8624 (2017).
31. Wang, Z. et al. Understanding the roles of oxygen vacancies in hematite-based photoelectrochemical processes. *Angew. Chem. Int. Ed.* **58**, 1030–1034 (2019).
32. Jin, L., Li, F. & Zhang, S. J. *J. Am. Ceram. Soc.* **97**, 1–27 (2014).
33. Chen, P. et al. In situ growth of 2D perovskite capping layer for stable and efficient perovskite solar cells. *Adv. Funct. Mater.* **28**, 1706923 (2018).
34. Zhang, Z. & Yates, J. T. Jr. Band bending in semiconductors: chemical and physical consequences at surfaces and interfaces. *Chem. Rev.* **112**, 5520–5551 (2012).
35. Henck, H. et al. Interface dipole and band bending in the hybrid p-n heterojunction MoS_2/GaN (0001). *Phys. Rev. B* **96**, 115312 (2017).
36. Wang, Z. et al. Identifying copper vacancies and their role in the CuO based photocathode for water splitting. *Angew. Chem. Int. Ed.* **58**, 17604–17609 (2019).
37. Živković, A. & de Leeuw, N. H. Exploring the formation of intrinsic p-type and n-type defects in CuO . *Phys. Rev. Mater.* **4**, 074606 (2020).
38. Li, X. et al. Oxygen vacancy: how will poling history affect its role in photoelectrocatalysis. *ChemSusChem* **20**, e202400946 (2024).
39. Ab Rahim, M. H. et al. Oxidation of methane to methanol with hydrogen peroxide using supported gold–palladium alloy nanoparticles. *Angew. Chem. Int. Ed.* **52**, 1280–1284 (2013).
40. Freakley, S. J. et al. Methane oxidation to methanol in water. *Acc. Chem. Res.* **54**, 2614–2623 (2021).
41. Mostaghimi, A. H. B., Al-Attas, T. A., Kibria, M. G. & Siahrostami, S. A review on electrocatalytic oxidation of methane to oxygenates. *J. Mater. Chem. A* **8**, 15575–15590 (2020).
42. Wu, Y., Jiang, Z., Lu, X., Liang, Y. & Wang, H. Domino electroreduction of CO_2 to methanol on a molecular catalyst. *Nature* **575**, 639–642 (2019).
43. Woo, H. K. et al. Defect engineering of WO_3 by rapid flame reduction for efficient photoelectrochemical conversion of methane into liquid oxygenates. *Nano Lett.* **23**, 11493–11500 (2023).
44. Li, W. et al. Selective CO Production by Photoelectrochemical Methane Oxidation on TiO_2 . *ACS Cent. Sci.* **4**, 631–637 (2018).
45. Kresse, G. & Furthmüller, J. Efficiency of ab-initio total energy calculations for metals and semiconductors using a plane-wave basis set. *Comput. Mater. Sci.* **6**, 15–50 (1996).
46. Kresse, G. & Furthmüller, J. Efficient iterative schemes for ab initio total-energy calculations using a plane-wave basis set. *Phys. Rev. B* **54**, 11169 (1996).
47. King-Smith, R. & Vanderbilt, D. Theory of polarization of crystalline solids. *Phys. Rev. B* **47**, 1651 (1993).
48. Vanderbilt, D. & King-Smith, R. Electric polarization as a bulk quantity and its relation to surface charge. *Phys. Rev. B* **48**, 4442 (1993).
49. Momma, K. & Izumi, F. VESTA 3 for three-dimensional visualization of crystal, volumetric and morphology data. *J. Appl. Crystallogr.* **44**, 1272 (2011).
50. Qi, Y. et al. Unraveling of cocatalysts photodeposited selectively on facets of BiVO_4 to boost solar water splitting. *Nat. Commun.* **13**, 484 (2022).

51. Kuang, Y. et al. A front-illuminated nanostructured transparent BiVO₄ photoanode for > 2% efficient water splitting. *Adv. Energy Mater.* **6**, 1501645 (2016).

Acknowledgements

The authors would like to acknowledge the support by Australian Research Council through its DECRA (DE210100930, DE230101712), Discovery (DP200101900, DP230100462), Future Fellowship (FT230100251) and Laureate Fellowship (FL190100139) schemes. This work was performed in part at the Queensland node of the Australian National Fabrication Facility. This research was undertaken on the X-ray Absorption Spectroscopy and Soft X-ray Absorption Spectroscopy beamlines at the Australian Synchrotron, part of ANSTO. A company established under the National Collaborative Research Infrastructure Strategy to provide nano and microfabrication facilities for Australia's researchers. The authors acknowledge the facilities, and the scientific and technical assistance, of the Australian Microscopy and Micro-analysis Research Facility at the Centre for Microscopy and Micro-analysis, The University of Queensland. X. L., J. Y. and Y. B. acknowledge scholarship support from UQ Graduate School.

Author contributions

L.W. and Z.W. supervised the study and nucleated the research concept. X.L. completed the photoelectrodes fabrication and photoelectrocatalytic test. Z.W. and X.L. analyzed the results and prepared the manuscript. A.S. and A.B. implemented the computational work. K.W. assisted the NMR data collection. P.C. and K.W. assisted the NMR data analysis. H.L. and J.Y. assisted the X-ray absorption spectra data. P.C. assisted the TRPL data collection and analysis. Y.B. assisted the photoelectrocatalytic methane oxidation test. S.Z. and G.L. provided constructive comments and suggestions on the defect dipoles concept and roles. All the authors contributed to manuscript polishing and discussion.

Competing interests

The authors declare no competing interests.

Additional information

Supplementary information The online version contains supplementary material available at <https://doi.org/10.1038/s41467-024-53426-8>.

Correspondence and requests for materials should be addressed to Zhiliang Wang or Lianzhou Wang.

Peer review information *Nature Communications* thanks Yongbo Kuang and the other anonymous reviewer(s) for their contribution to the peer review of this work. A peer review file is available.

Reprints and permissions information is available at <http://www.nature.com/reprints>

Publisher's note Springer Nature remains neutral with regard to jurisdictional claims in published maps and institutional affiliations.

Open Access This article is licensed under a Creative Commons Attribution-NonCommercial-NoDerivatives 4.0 International License, which permits any non-commercial use, sharing, distribution and reproduction in any medium or format, as long as you give appropriate credit to the original author(s) and the source, provide a link to the Creative Commons licence, and indicate if you modified the licensed material. You do not have permission under this licence to share adapted material derived from this article or parts of it. The images or other third party material in this article are included in the article's Creative Commons licence, unless indicated otherwise in a credit line to the material. If material is not included in the article's Creative Commons licence and your intended use is not permitted by statutory regulation or exceeds the permitted use, you will need to obtain permission directly from the copyright holder. To view a copy of this licence, visit <http://creativecommons.org/licenses/by-nc-nd/4.0/>.

© The Author(s) 2024